Earth and Planetary Science Letters 449 (2016) 164–175

Contents lists available at ScienceDirect

Earth and Planetary Science Letters

www.elsevier.com/locate/epsl

Layered structure in the upper mantle across North America from joint inversion of long and short period seismic data

M. Calò [a,*,1], T. Bodin [a,2], B. Romanowicz [a,b,c]

[a] Berkeley Seimological Laboratory, 215 McCone Hall, UC Berkeley, Berkeley CA 94720-4760, USA
[b] Insitut de Physique du Globe de Paris (IPGP), 1 Rue Jussieu, F-75005 Paris, France
[c] College de France, 11 place Marcelin Berthelot, F-75231 Paris, France

ARTICLE INFO

Article history:
Received 13 January 2016
Received in revised form 29 May 2016
Accepted 30 May 2016
Available online xxxx
Editor: P. Shearer

Keywords:
mid-lithosphere discontinuity
Lithosphere–Asthenosphere Boundary
Lehmann discontinuity
mantle structure
Bayesian inversion

ABSTRACT

We estimate crustal and uppermost mantle shear velocity structure beneath 30 stations in North America by jointly inverting the high frequency scattered wavefield observed in the P wave coda, together with long period surface wave phase and group dispersion data. Several features distinguish our approach from previous such joint inversions. 1) We apply a cross-convolution method, rather than more standard deconvolution approaches used in receiver function studies, and consider both Love and Rayleigh wave dispersion, allowing us to infer profiles of radial anisotropy. 2) We generate probabilistic 1D radially anisotropic depth profiles across the whole uppermost mantle, down to ~350 km depth. 3) The inverse problem is cast in a trans-dimensional Bayesian formalism, where the number of isotropic and anisotropic layers is treated as unknown, allowing us to obtain models described with the least number of parameters. Results show that the tectonically active region west of the Rocky Mountain Front is marked by a Lithospheric Asthenosphere Boundary and a Lehmann Discontinuity occurring at relatively shallow depths (60–150 km and 100–200 km, respectively), whereas further east, in the stable craton, these discontinuities are deeper (170–200 km and 200–250 km, respectively). In addition, in the stable part of the continent, at least two Mid-Lithospheric Discontinuities are present at intermediate depths, suggesting the existence of strong lithospheric layering, and a mechanism for lithospheric thickening by underplating of additional layers as cratonic age increases. The Moho across the continent as well as mid-crustal discontinuities in the craton are also imaged, in agreement with independent studies.

1. Introduction

Different seismological approaches have been used to image crustal and lithospheric structure at continental scales, in particular in North America (NA). At long periods (20–250 s), surface wave tomography provides resolution of volumetric heterogeneity down to ~300 km depth, at scales down to ~500 km laterally, and ~50 km vertically (van der Lee and Frederiksen, 2005; Nettles and Dziewoński, 2008; Yuan et al., 2014; French and Romanowicz, 2014; Schaeffer and Lebedev, 2014). However, surface waves cannot uniquely resolve sharp interfaces, such as the Moho, the Lithosphere–Asthenosphere Boundary (LAB), the Lehmann discontinuity (L) or Mid-Lithospheric-Discontinuities (MLD's). In order to image such discontinuities, methods based on the analysis of the scattered wavefield at shorter periods (10–30 s) have been developed. The most frequently considered method uses information contained in phases converted at crust and upper mantle interfaces under single stations, the so-called receiver function method (RF, Vinnik, 1977; Ammon et al., 1990; Bostock, 1998).

The densification of broadband stations in NA (e.g. USArray) has made it possible to construct dense RF profiles across much of the conterminous US (e.g. Kumar et al., 2012; Hansen et al., 2015), confirming the first order striking differences in deep structure previously observed from tomography, between the tectonically active western US and the central craton (Marone and Romanowicz, 2007; Nettles and Dziewoński, 2008), with a rather sharp transition between them that roughly follows the Rocky Mountain Front (RMF, Fig. 1). West of this boundary, the crust is thinner, and a prominent negative boundary at depths between 60–80 km is generally interpreted as the LAB (Abt et al., 2010). East of this bound-

* Corresponding author.
E-mail addresses: calo@geofisica.unam.mx, marcoocalo@yahoo.it (M. Calò).
[1] *Now at*: Instituto de Geofísica, Universidad Nacional Autónoma de México (UNAM), Circuito de la Investigación Científica s/n, Ciudad Universitaria, Delegación Coyoacán, C.P. 04510, México D.F.
[2] *Now at*: Univ. Lyon, Université Lyon 1, Ens de Lyon, CNRS, UMR 5276 LGL-TPE, F-69622, Villeurbanne, France.

http://dx.doi.org/10.1016/j.epsl.2016.05.054
0012-821X/

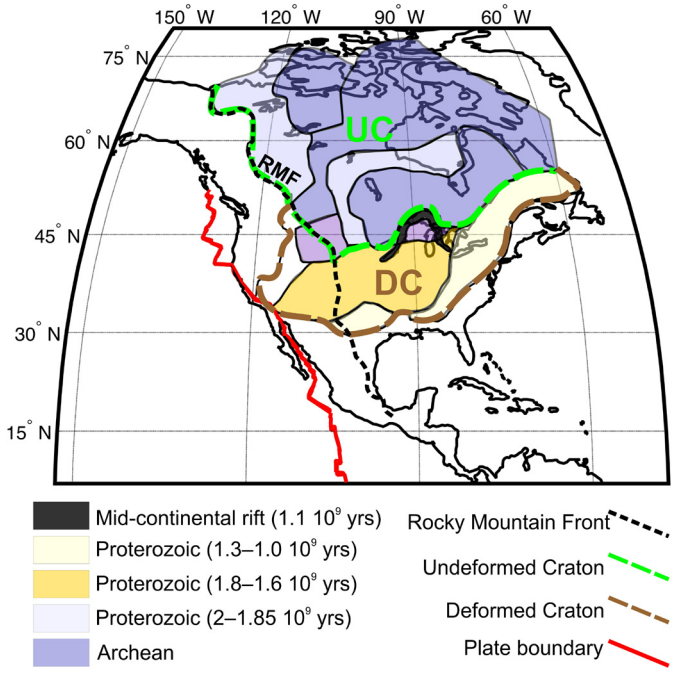

Fig. 1. Precambrian basement age in the North American continent simplified from Whitmeyer and Karlstrom (2007). Red line marks the plate boundaries and black dashed line indicates the Rocky Mountain Front (RMF). Green dashed line limits the undeformed craton (UC) and brown dashed one the deformed craton (DC). (For interpretation of the references to color in this figure legend, the reader is referred to the web version of this article.)

ary, the crust is thick, and the lithosphere reaches 200–250 km depth, as determined from global and continental scale seismic tomography. Moreover, anisotropic tomography combining long period waveforms with SKS splitting data has allowed the mapping of the LAB as a rapid change in the direction of the fast axis of anisotropy with depth, towards the absolute plate motion (APM) direction (e.g. Marone and Romanowicz, 2007; Yuan and Romanowicz, 2010). On the other hand, the LAB has not been detected consistently in the craton from RF studies, leading to its interpretation as a relatively gradual transition of primarily thermal nature (e.g. Abt et al., 2010), although recent studies based on USArray data seem to resolve it more clearly (Kumar et al., 2012; Hansen et al., 2015).

The presence of layering within the continental lithosphere has long been known (e.g. Hales, 1969) and confirmed from the analysis of long range seismic profiles, which showed the presence of a zone of scattering and lower seismic velocities starting at about 100 km depth in cratons, defining the so-called "8° discontinuity" (Thybo and Perchuc, 1997). Layering has also been found in scattering studies (e.g. Bostock, 1998) and the presence of negative discontinuities in the mid-lithosphere was clearly demonstrated in recent RF studies across the NA craton (Abt et al., 2010; Rychert et al., 2010; Kumar et al., 2012; Hansen et al., 2015). Interestingly, an MLD with large topographic variations in the depth range 100–160 km is detected by a rapid change in the fast axis direction of anisotropy (e.g. Yuan and Romanowicz, 2010).

At depths greater than 200 km, regional studies suggest the existence of additional reflectors such as the discontinuity discovered by Lehmann (1961). We refer to it as the "L" discontinuity in what follows. Generally, it is attributed to a petrologically distinct chemical boundary under continental cratons (Gu et al., 2001). Leven et al. (1981) suggest that the L corresponds to a change in the orientation of the fast axis of azimuthal anisotropy. However Vinnik et al. (2005) argue that seismic anisotropy plays a minor role in its origin.

The nature of the L, LAB and MLD(s) across NA remains a subject of vigorous debate, and different interpretations have been proposed as to their significance with respect to the formation of the cratonic lithosphere.

Although the RF approach provides information on fine-scale structure, this method presents several drawbacks: 1) lateral variations in the depth of discontinuities trades off with that of volumetric heterogeneity in the shallow mantle and crust (e.g. Ammon et al., 1990). Since the depth of discontinuities is generally determined through migration in a 1D earth model, their topography may be affected by unaccounted for velocity anomalies above them; 2) the imaged lithospheric discontinuities, especially in the case of P-to-s receiver functions, can be polluted by the strong signal from crustal reverberations, particularly in the depth of interest for continental lithospheric studies.

Since surface wave data and RFs provide complementary constraints on shallow earth structure, it is natural to try and combine them to obtain more robust models of the crust and uppermost mantle (e.g. Julià et al., 2000). This approach has recently gained momentum, in particular for constraining the depth of the Moho (e.g. Julià et al., 2000; Shen et al., 2013; Agrawal et al., 2015). Forward modeling approaches using a Monte Carlo Markov Chain (MCMC) framework (Sambridge and Mosegaard, 2002) have been developed for this purpose and applied in particular in NA (e.g. Shen et al., 2013), where the density of USArray stations combined with ambient noise tomography provides high-resolution 3D models of the crust and uppermost mantle.

In this work we apply a similar approach, albeit extended to a larger depth range, and jointly invert a combination of body wave data (scattered phases) and longer period surface wave dispersion data, in order to simultaneously investigate lateral variations in velocity and in the depth of upper mantle discontinuities in NA. There are several original aspects to our approach: 1) we consider both Love and Rayleigh wave dispersion data, allowing us to include radial anisotropy in our inversion; 2) instead of a standard RF methodology, our body wave dataset derives directly from seismic waveforms through a cross-convolution method (Bodin et al., 2014), avoiding the instabilities arising from deconvolution, and, importantly, allowing us to take into account crustal multiples without ambiguity; 3) we use a trans-dimensional MCMC approach in which the number of isotropic and anisotropic layers is treated as unknown, allowing us to obtain models with the least number of parameters compatible with the data (Bodin et al., 2014). In contrast to standard RF analysis, our approach allows us to constrain not only the position of discontinuities, but also the isotropic and anisotropic variations of shear velocity between them, in particular providing better constraints on the characteristics of the intra-lithospheric layers. Furthermore, the trans-dimensional parameterization allows us to account for the trade-off between layering, and radial anisotropy when jointly inverting Love and Rayleigh waves (Bodin et al., 2015).

Our forward modeling approach is based on a direct parameter search where a large number of Earth models are tested against the data, making it much more expensive computationally than standard RF migration schemes. Furthermore, increasing the period range of the surface waves data and the duration of the waveforms to investigate deeper structure also increases the computational burden with respect to other MCMC studies (e.g. Shen et al., 2013). It is therefore impractical to apply it to every single USArray station, at least for the moment. Instead, as a first step, we apply it to a subset of ∼30 selected stations that are representative of the large-scale lateral variations of structure in NA. In order to select the stations to represent contrasted structures across NA, we started from a recently developed high resolution global radially anisotropic shear velocity model of the mantle, to which we applied a cluster analysis method, to objectively define three distinct

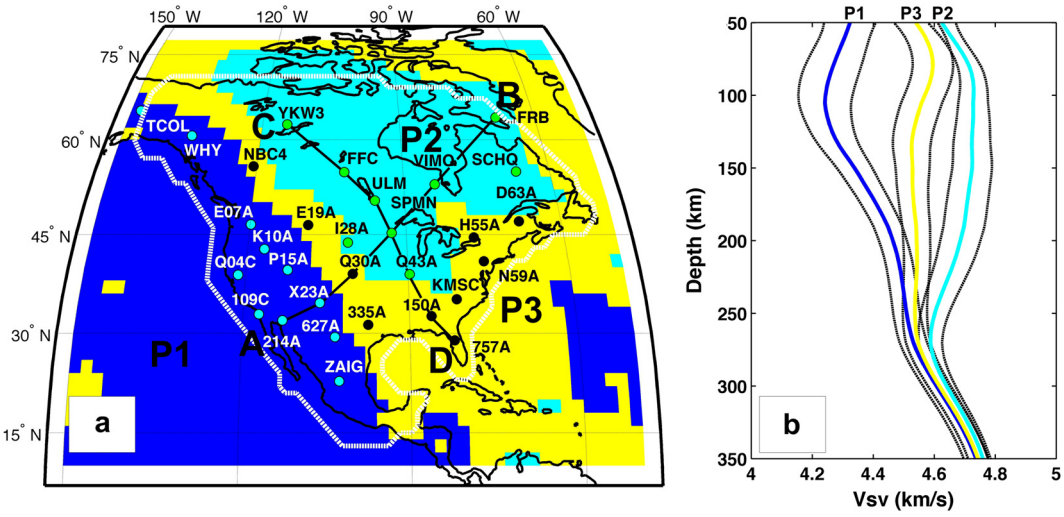

Fig. 2. a) Geographic extent of the 3 regions (P1, P2 and P3) identified using k-means clustering with N = 3 applied to model SEMUMCB-WM1 (French and Romanowicz, 2014). A–B and C–D are the locations of the profiles shown in Fig. 7 and Appendix 2. White dashed line limits the study region. The position and name of the stations used to calculate the 1D probabilistic profiles are also shown. b) 1D V_{sv} profiles of SEMUMCB-WM1 (colored lines) in the study region (inside the white line on map) and their standard deviations (in black). (For interpretation of the references to color in this figure legend, the reader is referred to the web version of this article.)

regions across the continent, in which the shear velocity variations with depth are similar, to first order. As previously found in the global case (Lekic and Romanowicz, 2011), these regions correspond well with surface geology (Fig. 1 and Fig. 2a). We then picked about 10 stations for which high quality data are available, in each region, and performed our analysis at these stations.

In what follows, we successively present the results of cluster analysis applied to the tomographic model, the forward modeling approach used to derive 1D probabilistic layered radially anisotropic structure, the datasets considered, and finally the results at each station. We compare structures obtained at different stations, finding similarities within each region that justify the a-priori regionalization based on the tomographic model. This brings out characteristic features of lithosphere and asthenosphere layering across the continent, and in particular the presence of intra-lithospheric layering beneath the craton. We discuss our findings and their implications in the light of published results based on either tomography or standard RF approaches.

2. Regionalization by cluster analysis

We applied cluster analysis (ClAn) over the region of interest to a recent global radially anisotropic shear velocity model constructed using the Spectral Element Method (SEM) (SEMUCB-WM1, French and Romanowicz, 2014). Fig. 1 shows a simplified geological map of NA, displaying the undeformed part of the NA craton (UC), the deformed one (DC), and the Rocky Mountain Front (RMF) separating the tectonically active western US from the central craton, together with the age of the main units.

As shown in Lekic and Romanowicz (2011), cluster analysis of upper mantle models provides an objective way to characterize regions of similar tectonic character, using a small number of clusters (N ∼ 3–8). In particular, at the global scale, the use of k-means clustering of isotropic velocity-depth profiles down to 300 km brings out the global distribution of cratons, characterized by thick (∼200 km) and fast lithosphere, and a mildly marked upper mantle low velocity zone.

The k-means clustering with N = 3 applied to the region of study (longitude 55–150W and latitude 10–78N, Fig. 2a), in the depth range 50–350 km, yields contiguous regions that reflect well what we know from geology: the NA craton is described by one cluster (P2), and a second cluster includes the tectonic west and the ocean region to the west of it (P1). The transition region across the RMF, as well as the southern and eastern US fall into a third cluster (P3).

We performed tests to assess the number of regions in which the NA continent needs to be divided to obtain a first order description of the lithospheric pattern. We verified that, from N = 3 to N = 5, the cluster analysis provides similar information. A number of clusters larger than 3 adds details only in cluster P3. Only when N is greater than 5, we obtain separation of the P1 and P3 regions, providing second order details. Furthermore, in order to assess the robustness of the regionalization, we applied the ClAn to other global shear velocity models (Kustowski et al., 2008; Ritsema et al., 2011; Lekic and Romanowicz, 2011), finding similar regionalizations. We therefore consider the separation into 3 provinces as a robust and objective regionalization of the study region, to the first order.

Fig. 2b shows the shear velocity (V_{sv}) depth profiles corresponding to each cluster, as well as their averages by cluster and the corresponding standard deviations. We recover: a) the well known contrast between the thick (∼200 km) and fast lithosphere of the craton (P2) and, b) the thin lithosphere (<100 km) and well developed low velocity zone in the western US and adjacent ocean (P1), with a minimum around 100 km on average, c) a lithosphere of intermediate thickness, and a slightly marked, deeper LVZ (around 125 km on average) in the intermediate cluster region (P3).

3. Method: inferring layered structure at a selected subset of stations

Here, we describe our approach to jointly invert fundamental mode Love and Rayleigh wave dispersion curves (SWD) and P-to-s converted phase data beneath a given station.

3.1. Data

For each station we use the following datasets:

1) Rayleigh and Love group velocity dispersion curves in the period range 16 s to 150 s, extracted from the global models of Shapiro and Ritzwoller (2002) at the location of each of our stations.

2) Rayleigh and Love phase velocity dispersion curves in the period range 25 s to 250 s, extracted from the global models of Ekström (2011).

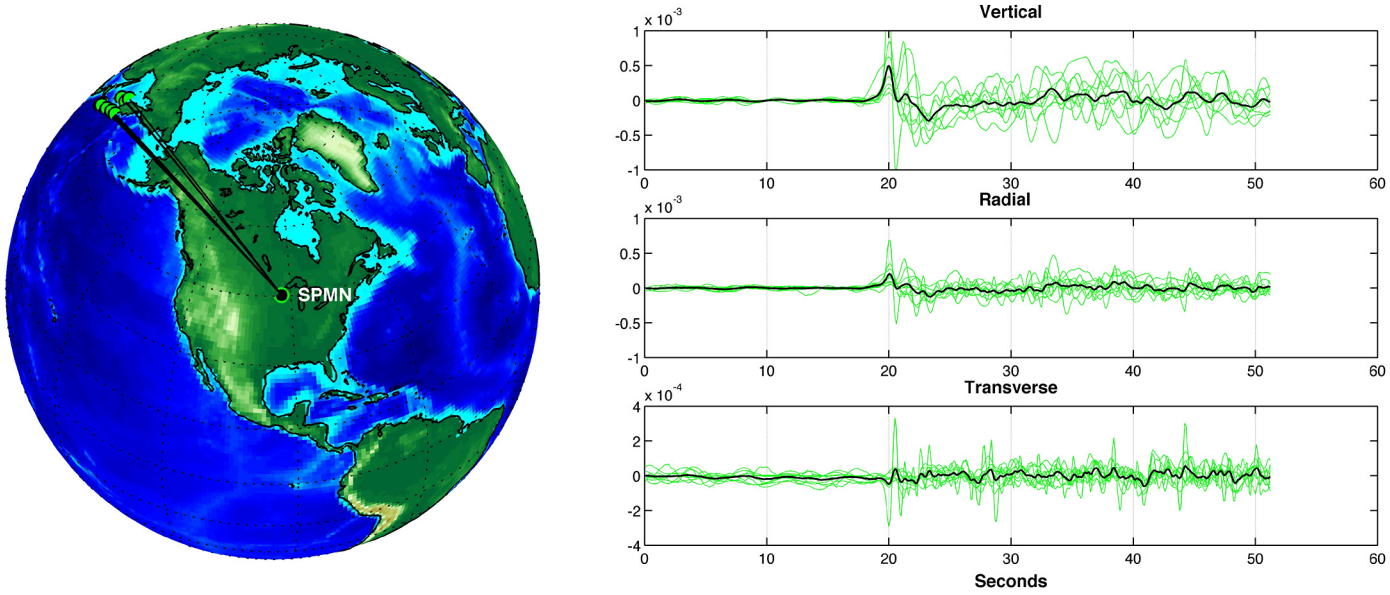

Fig. 3. Left: ray paths of the events recorded at station SPMN to construct the average waveform. Right: single (green) and stacked (black) waveforms used for the MCMC inversion. (For interpretation of the references to color in this figure legend, the reader is referred to the web version of this article.)

We recognize that these "data" are the result of global tomographic inversions, and hence are not free from artifacts due to regularization and linearization that can partially bias the results of the inversion.

3) Vertical and radial component body waveforms in the period range 10–30 s recorded at each station. Instead of deconvolving the vertical component from the radial one, as done in standard RF analysis (Vinnik, 1977), here we directly invert the 2 component seismograms using a cross-convolution method as described in Bodin et al. (2014). The dataset consists of waveforms generated after stacking records of at least 10 events of magnitude ranging between Mw = 5.5 and Mw = 7.6 (Fig. 3), obtained from the IRIS database. In order to avoid move-out and 3D effects, events stacked at each station are selected within a narrow distance and back-azimuth (<10°, Fig. 3). The spatial windows are selected for station-cluster distances in the range 40°–88°.

During the selection procedure, we only kept events for which the signal-to-noise ratio is higher than 15 (considering the maximum amplitude of the first P arrival). For the inversion, we consider the first 32 s of the signal to isolate the response of the crust and upper mantle down to 200–300 km depth. We also correct for instrument response before rotating the horizontal components to radial and transverse. Stacks are constructed by following the approach of Shearer (1991). Seismograms are aligned to the maximum amplitude of the first P arrival, and summed in the time domain (Fig. 3). We also perform a sign equalization to insure that all events have the same polarity. Thus, the observations at each station simply consist of two waveforms that can be written as:

$$V(t) = \Sigma V_i(t) = \Sigma\left[v(\mathbf{m},t) * s_i(t) + \varepsilon_i(t)\right]$$
$$= v(\mathbf{m},t) * \Sigma s_i(t) + \Sigma\varepsilon_i(t)$$
$$H(t) = \Sigma H_i(t) = \Sigma\left[h(\mathbf{m},t) * s_i(t) + \varepsilon_i(t)\right]$$
$$= h(\mathbf{m},t) * \Sigma s_i(t) + \Sigma\varepsilon_i(t)$$

where $V_i(t)$, and $H_i(t)$ are the vertical and horizontal components of individual events, which can be decomposed as the convolution of the impulse Earth responses $v(\mathbf{m},t)$ and $h(\mathbf{m},t)$, respectively, with the source time functions $s_i(t)$. Since we choose events coming from a narrow range in distance and back-azimuth, the Green's functions v and h are assumed to be similar for all events, and can be taken out of the sum. This allows us to reduce the amount of incoherent noise, as the term $\Sigma\varepsilon_i(t)$ tends to zero as we add more events. The size of the distance-back-azimuth range for which events are collected needs to be carefully chosen, as there is a trade-off between theoretical errors due to 3D effects (as the bin gets larger, the Earth response $v(\mathbf{m},t)$ and $h(\mathbf{m},t)$ for each event changes), and random noise $\Sigma\varepsilon_i(t)$ which depends on the number of events stacked.

An inherent problem is that the inverted structure only represents the volume sampled by the rays, and not the average structure immediately under the station. This can be addressed by averaging data collected over a wide range of azimuths, via harmonic decomposition (e.g. Girardin and Farra, 1998; Bianchi et al., 2010 and reference therein). However in Appendix 1 we show, through tests performed at three stations, that the structure recovered using our simplified approach is only marginally biased by structural variations between different azimuth/distance bins. Still, biases due to limited azimuthal coverage could be present at some stations, especially for anisotropy, a computationally demanding issue we will investigate in the future, when we apply this methodology to a larger dataset and also solve for azimuthal anisotropy (e.g. Bodin et al., 2016).

3.2. Inversion methodology for 1D layered depth profiles

The algorithm developed here consists in a joint inversion of the different data types described in the previous section. At each station, the solution is a probabilistic 1D profile of shear wave velocity of vertically polarized waves (V_{sv}) and radial anisotropy ($\xi = (V_{sh}/V_{sv})^2$). Below, we briefly present the method. For a more detailed description, we refer the reader to Bodin et al. (2012, 2014, 2016). In Appendix 1, we present synthetic tests showing the ability of the method to resolve seismic structures down to 350 km beneath individual stations.

3.2.1. Model parameterization

We use a trans-dimensional Bayesian scheme where the number of layers is considered as variable in the inversion. Furthermore, instead of inverting for 2 parameters in each layer (i.e. V_{sv} and ξ), we expand the trans-dimensional formalism a step further and let the data decide whether anisotropy is required in

each layer. That is, the number of parameters in each layer (1 for isotropic layers and 2 for anisotropic layers) is also treated as an unknown parameter. The parsimonious character of the Bayesian inversion gives preference to models with the least number of parameters (i.e. least number of layers, and maximum number of isotropic layers).

We assume a vertical transverse isotropic (VTI) medium, i.e. with an elastic tensor with vertical axis hexagonal symmetry. The level of radial anisotropy is thus described by $\xi = (V_{sh}/V_{sv})^2$. Under each station, the unknown seismic model $[V_{sv},\ \xi]$ is parameterized in terms of perturbations $[\delta V_{sv} = (V_{sv} - V_{sv}^0)/V_{sv}^0,\ \delta\xi = (\xi - \xi_i^0)/\xi^0]$ from a fixed isotropic background model $[V_{sv}^0,\ \xi^0 = 1]$. These perturbations do not need to be small, as there is no linearization involved in the inversion. The three other anisotropic parameters and density are then obtained at each depth using empirical scaling laws (e.g. Panning and Romanowicz, 2006 and references therein). A stack of layers with constant seismic velocity defines both the background model and the perturbed model. The background model allows us to impose discontinuities that will remain fixed during the inversion (410, and 670 discontinuity, etc.). The perturbed model is unknown in the problem; it has a variable number of layers, and each layer can be either isotropic and solely described by δV_{sv}, or anisotropic (and described by two unknown parameters: δV_{sv} and $\delta\xi$). The thickness of layers is also variable, and the bottom layer is a half-space. A reversible-jump Monte Carlo algorithm is used to explore different parameterizations. A random walk explores the model space with five different types of perturbations: 1) changing the depth of a discontinuity; 2) adding an isotropic layer; 3) changing the isotropic velocity of a layer; 4) adding anisotropy to an isotropic layer; 5) changing the amplitude of anisotropy of an anisotropic layer.

At each step of the random walk, a new model is proposed and data are estimated for this model. SWD is computed in a fully non-linear fashion by normal mode summation in a spherical Earth with a Runge–Kutta matrix integration (Takeuchi and Saito, 1972). For body waves, the impulse response of a model to an incoming planar wave is computed with a reflectivity scheme (Levin and Park, 1998).

3.2.2. Bayesian inference

The problem is cast in a Bayesian framework, where unknown model parameters are treated as random variables, and described with probability distributions. The solution to the problem is given by the Posterior Probability Distribution (PPD), defined as the probability of model $\mathbf{m}$, given the observations $\mathbf{d}$. The PPD combines data constraints (through the likelihood probability density function) with prior information (independent of the data):

$$p(\mathbf{m} \mid \mathbf{d}) = p(\mathbf{m})p(\mathbf{d} \mid \mathbf{m})$$

$$\text{posterior} = \text{prior } x \text{ likelihood}$$

3.2.3. The likelihood

Assuming that different data types are measured independently, we can write the likelihood as a product of the likelihoods for each data type:

$$p(\mathbf{d} \mid \mathbf{m}) = p(\mathbf{d}_{swd} \mid \mathbf{m})p(\mathbf{d}_{RF} \mid \mathbf{m})$$

For SWD, the likelihood is simply given by a Gaussian probability distribution around the observed data vector:

$$p(\mathbf{d}_{swd} \mid \mathbf{m}) = \frac{1}{(\sqrt{2\pi}\sigma_1)^n} exp^{\left(\frac{-(\mathbf{d}_{swd} - \mathbf{d}_{est}(m))^2}{2\sigma_1^2}\right)}$$

where n is the number of data points, $\mathbf{d}_{est}(\mathbf{m})$ the dispersion curve estimated for a model $\mathbf{m}$, and σ_1 the standard deviation of data errors.

For converted waves, we use a cross-convolution misfit function (Menke and Levin, 2003; Bodin et al., 2014) based on the following vector of residuals:

$$\Phi(t, \mathbf{m}) = H(t) * v(t, \mathbf{m}) - V(t) * h(t, \mathbf{m})$$

where $[H(t)\ V(t)]$ are components of the observed stacked seismogram, and $[h(t, \mathbf{m})\ v(t, \mathbf{m})]$ are the Earth's impulse response function (or green's function) for model $\mathbf{m}$. Assuming observations $[H(t)\ V(t)]$ are normally distributed random variables, and ignoring the correlation between components of vector $\Phi(t, m)$, we define a likelihood function from the distribution of the vector of residuals $\Phi(t, m)$:

$$p(\mathbf{d}_{rf} \mid \mathbf{m}) = \frac{1}{(\sqrt{2\pi}\sigma_2)^n} exp^{\left(\frac{|\Phi(\mathbf{m})|^2}{2\sigma_2^2}\right)}$$

Here we acknowledge that this is not an exact likelihood function, as it does not represent the distribution of the data, but rather the distribution of a vector of residuals conveniently defined. For a more rigorous approach, see Dettmer et al. (2015).

The variances of data errors σ_1^2 and σ_2^2 represent the level of information brought by each data type, which in the case of RFs and SWD can be difficult to quantify. In the case of a joint inversion, noise levels determine the weight given to each dataset in the inversion. Here we include σ_1^2 and σ_2^2 as unknowns in the inverse problem, using the so-called 'hierarchical Bayes' approach (Malinverno and Briggs, 2004).

3.2.4. The prior

In our trans-dimensional framework where the number of parameters is variable, the prior distribution penalizes overly complex models, i.e. those with many layers, or many anisotropic layers. We assume a uniform prior distribution for parameters V_{sv}, and ξ. For a given dimension (i.e. a given number of unknowns), the prior distribution integrates to one, and hence the *a priori* probability of a model becomes smaller as we add layers and increase the volume of the model space. This can be seen with the prior distribution on velocity values.

$$p(V) = p(V_1, V_2, \ldots, V_k) = \prod_{i=1}^{k} p(V_i) = \prod_{i=1}^{k} \frac{1}{V_{max} - V_{min}} = \left(\frac{1}{\Delta V}\right)^k$$

This shows that the prior probability decreases exponentially with the number of layers k, and hence acts as a penalizing term for overly complex models (and similarly for anisotropic parameters).

3.2.5. Sampling the posterior distribution

The PPD defined above is approximated by numerical integration with the reversible jump MCMC algorithm (Green, 1995). The algorithm is based on a direct parameter search scheme, where a large number of individual models with variable parameterizations are tested against the data.

Tests preformed using data calculated on finely layered anisotropic models show that the algorithm is suitable for jointly SWD and RF to properly retrieve the 1D earth structure beneath a station, and provide an estimation of the posterior error distribution (Appendix 1).

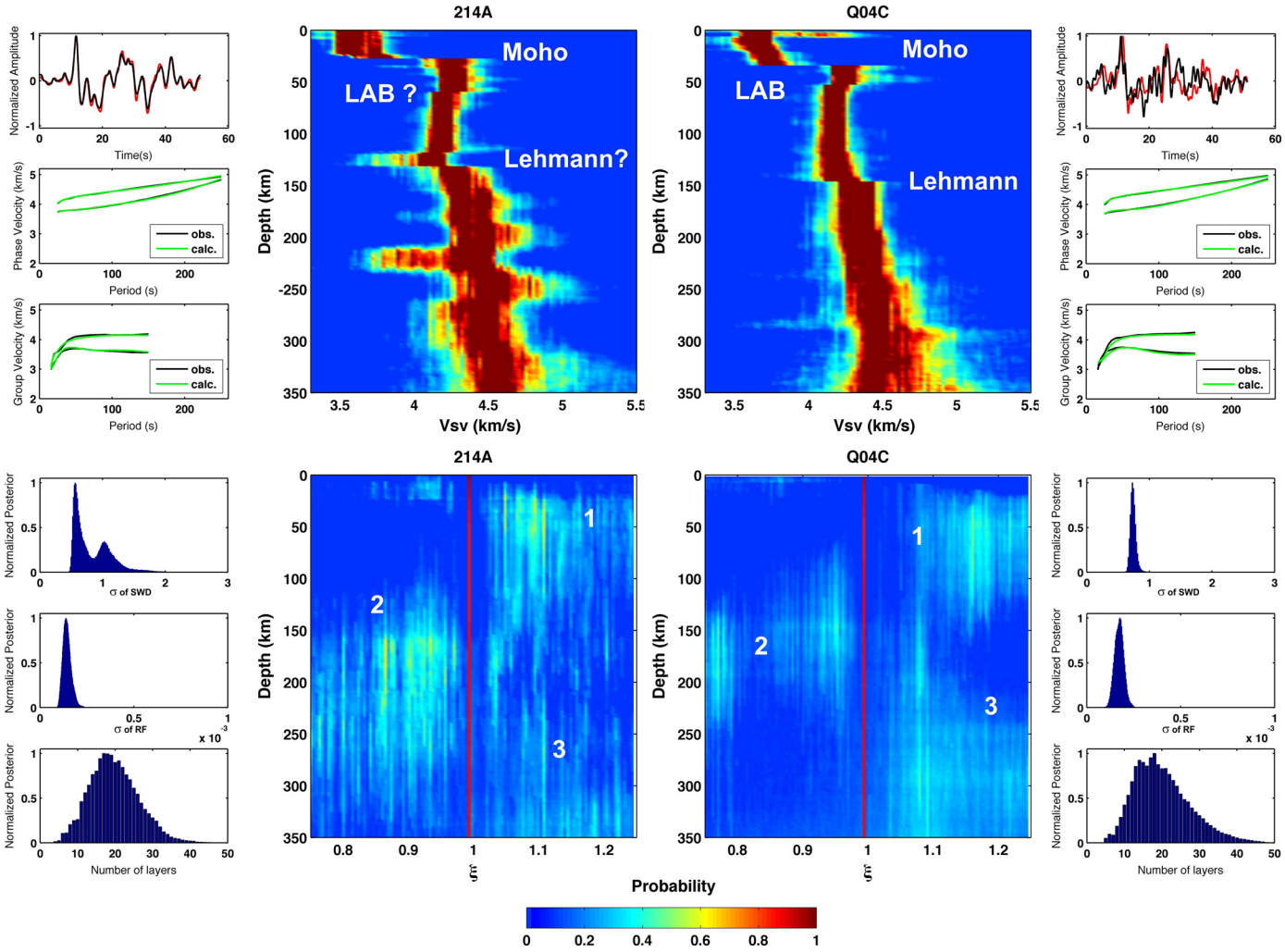

Fig. 4. Middle columns: Vertical shear velocity (top) and radial anisotropy distributions (bottom) at stations 214A and Q04C located in region P1 (see Fig. 2 for locations of stations). Color bars are normalized at each depth with respect to the corresponding mean value. We also show, for each station (left and right columns, respectively), from top to bottom: Cross-convolution receiver function of the best model (black: Z(obs)∗R(calc), red: Z(calc)∗R(obs)), comparison of the phase and group SWD of Rayleigh and Love Waves, posterior error distribution of the SWD and RF, and distribution of the number layers for all calculated models. (For interpretation of the references to color in this figure legend, the reader is referred to the web version of this article.)

4. 1D profiles beneath selected individual stations

The trans-dimensional inversion produces 1D probabilistic profiles of V_{sv} and ξ that allow us to identify several features of the crust and upper mantle of the NA continent. We group the 1D models according to the three provinces defined by the regionalization described above (P1 – western NA; P2 – craton; P3 – Rocky Mountain Front and southeastern US). We first show results at the two most representative stations of each province. Seismic profiles under other stations will be shown later in 2D profiles (Fig. 7, and Appendix 2) whereas the spatial distribution of discontinuities picked on the profiles is displayed in map view (Fig. 8). The results for all the 30 stations are also shown in Appendix 2. For each station we show probabilistic depth profiles for V_{sv} and ξ, as well as data fits for the best model in the ensemble solution, the inferred posterior distribution of errors in SWD (σ_1) and body waves (σ_2), and the distribution of the number of layers in the ensemble solution. The criteria for identifying discontinuities are the following: Only the discontinuities producing positive or negative velocity gradients (VG) greater than 1%, as calculated across a depth interval of 5 km, are considered (see Table T1, Appendix 3). The largest VG is associated with the Moho (VG > 8%), the deepest positive VG, where observed, is associated with the L discontinuity, and the deepest negative above the L with the LAB. Discontinuities (positive and negative) between the LAB and the Moho are associated with MLD's, whereas strong discontinuities above the Moho are intra-crustal ones (e.g. the Conrad).

4.1. Tectonic West (P1)

V_{sv} profiles in this region (Fig. 4, top) show: a) A positive discontinuity with VG generally greater than 11% at depths ranging from 28 km to 35 km that we interpret as the Moho; b) The presence of at least one negative discontinuity (VG = −2.55%) at 50–60 km depth interpreted as the LAB. Note that this discontinuity appears at greater depths beneath some other stations in region P1 (down to 130 km depth, see Fig. 8 and Appendix 2); c) At 140–150 km depth, a positive discontinuity (VG = 3.7%) that we interpret as the L; d) In the depth range 100–200 km, some profiles exhibit complexity (e.g. 214A located near the Baja California rift), which could be due to the presence of strong 3D heterogeneities in their vicinity, making it difficult to interpret individual 1D profiles.

Although not very well resolved, the distribution of radial anisotropy (Fig. 4, bottom) shows consistent patterns, with $\xi > 1$ reaching a maximum in the depth range 30–100 km (labels 1),

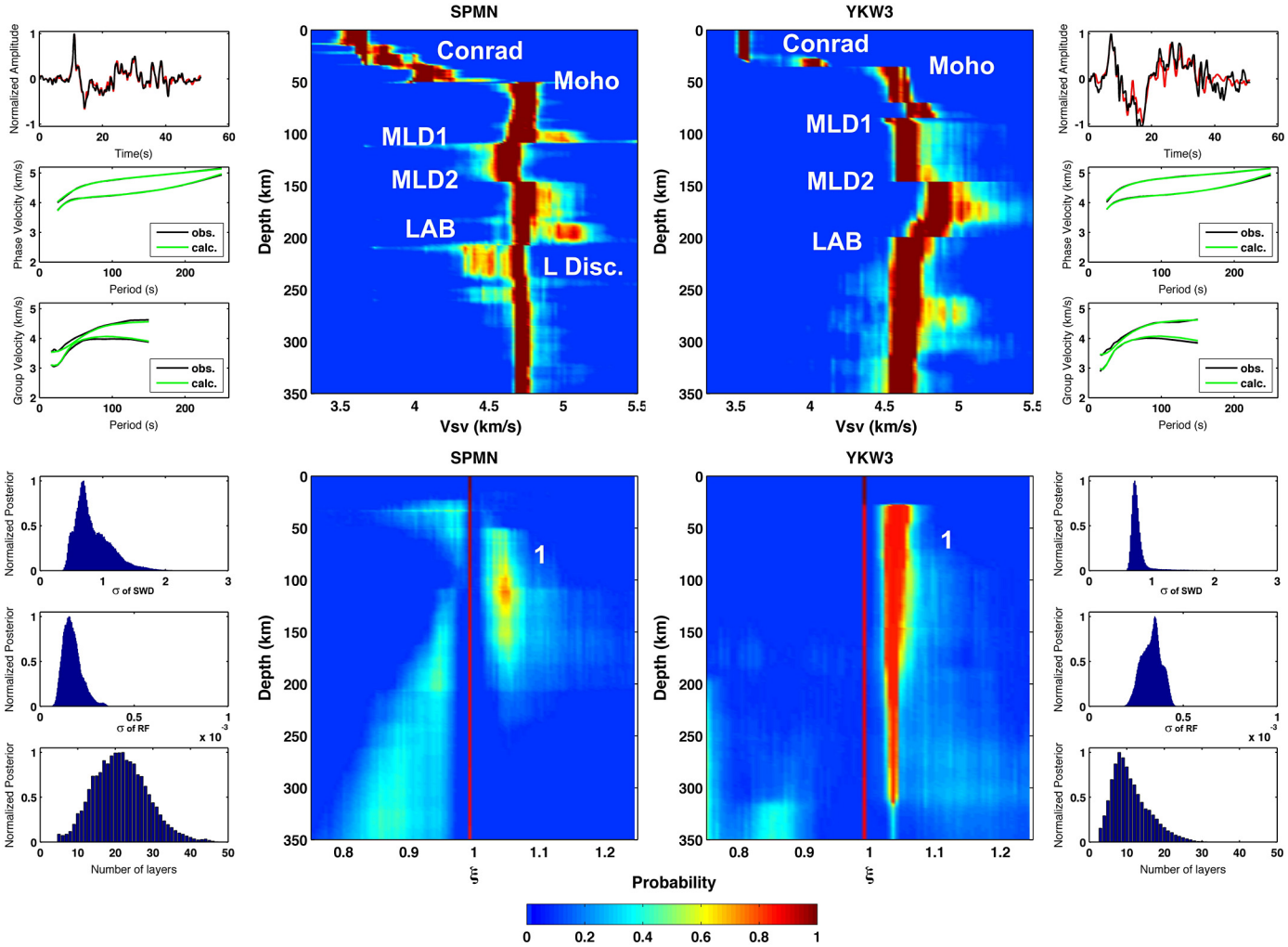

Fig. 5. Vertical V_{SV} distributions (top) and ξ distributions (bottom) at stations SPMN and YKW3 located in region P2 (locations of stations can be found in Fig. 2). For explanation of side panels, see Fig. 4.

$\xi < 1$ in the depth range 120–250 km (labels 2), and $\xi > 1$ again at greater depths (labels 3).

4.2. Craton (P2)

In this region, a deeper Moho with VG = 11.9% is found, ranging between 38 km and 50 km (Fig. 5). At mid-crustal depths (15–25 km), the profiles show at least one other positive discontinuity (VG = 6.6%) that we interpret as the Conrad discontinuity (Mueller and Landisman, 1966). Sometimes there is more than one mid-crustal discontinuity. At mantle depths, two clear negative discontinuities are present in the velocity profiles, marking the top of corresponding low velocity layers. The first one (MLD1) is observed at depths of 80–130 km (VG = −2.1%), whereas the second one (LAB) occurs at depths of 150–230 km (VG = −2.4%). These features are in agreement with the depth estimates, respectively, of the MLD and the LAB found by other authors (Abt et al., 2010, Yuan and Romanowicz, 2010; Hansen et al., 2015 and references therein). At intermediate depths (around 150 km), another mid-lithospheric discontinuity (MLD2, Fig. 5), marked by a positive jump in V_{SV} (HVD, High Velocity Discontinuity) is frequently found in our profiles with VG of about 3.6%. Below the LAB, not all the stations show a positive discontinuity that could be associated with the L, and generally, when it is present, it exhibits a VG = 2.0%, which is smaller than that observed in the other provinces, which have on average a VG of 3.3% (stations SPMN, ULM, FFC, Q43A, SCHQ). Interestingly, excluding the station I28A, we note the lack of an L discontinuity at stations located in the northernmost and easternmost part of the NA continent (e.g. YKW3, FRB, VIMO).

The ξ profiles are generally marked by $\xi > 1$ at depths greater than 30–60 km (labels 1). This pattern extends to variable depths, from 150 km to 350 km for the different stations suggesting a complex shape of the lower limit of the anisotropic layer, sometimes extending into the asthenosphere. This is in agreement with the observations made by other authors using different techniques (e.g. Nettles and Dziewoński, 2008; Yuan and Romanowicz, 2010).

4.3. Rocky Mountain Front and southeastern US (P3)

Stations located in this province show features that are intermediate between those of the two previous regions (Fig. 6). The Moho is observed at 35–45 km depth and several profiles show mid-crustal discontinuities (i.e. Conrad). The upper mantle profiles include one (e.g. E19A) or two (e.g. NBC4) discontinuities associated with the MLD and LAB. Some depth profiles also show the presence of intra-lithospheric HVD at depths of 100–150 km, while the L is found at 170–250 km.

Models of ξ also show mixed characteristics of P1 and P2. In Fig. 6, we show two stations with a ξ distribution with depth similar to that found in the craton, with positive values at depths ranging from 30–50 km down to 160–300 km (labels 1).

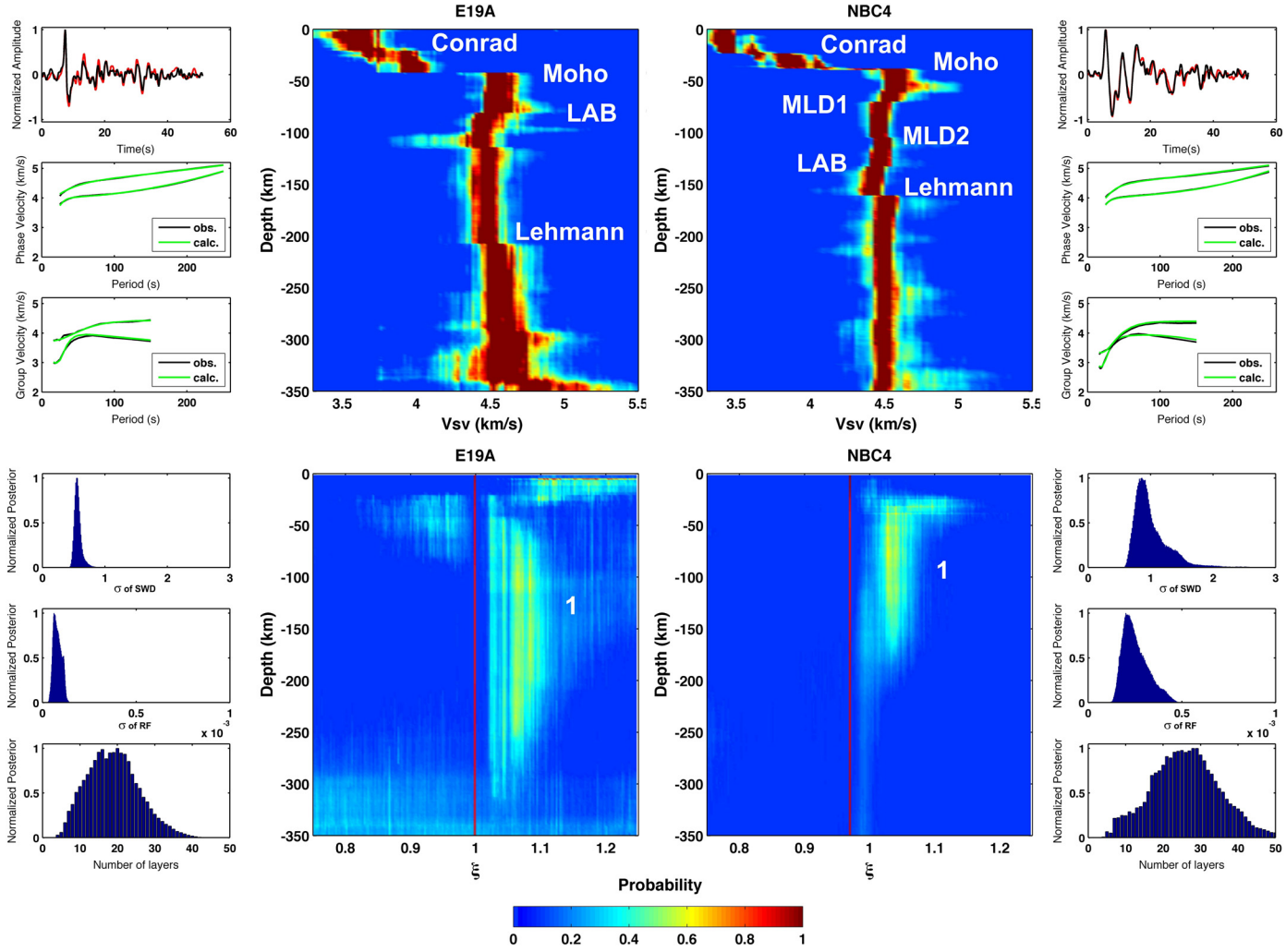

Fig. 6. Vertical V_{sv} distributions (top) and ξ distributions (bottom) at stations E19A and NBC4 located in region P3 (locations of stations can be found in Fig. 2). For explanation of side panels, see Fig. 4.

5. Lateral variations and 2D cross sections

Our probabilistic 1D profiles can also be grouped into 2D cross-sections spanning different provinces across the NA continent, along profiles A–B and C–D (Fig. 2), as shown in Fig. 7 and Appendix 2, respectively. The colored rectangles at the top of the section indicate which province (P1, P2, and P3) the profile belongs to. The positions of the main velocity discontinuities in depth have been manually picked and connected laterally to highlight possible trends in the topography of discontinuities.

5.1. Cross section A–B and spatial distribution of the major discontinuities

In Fig. 7 (profile A–B in Fig. 2) the Moho deepens from 28 km beneath station 214A (province P1), to ∼50 km beneath SPMN (province P2). The depth of the Moho beneath the other stations falling in P2 is always greater than 35–40 km, reflecting the large thickness of the crust in the craton. Furthermore, in P2, a mid-crustal discontinuity (i.e. the Conrad) is always present, as well as at least two velocity drops in the upper mantle. We interpret the first drop in V_{sv} in the upper mantle as the expression of an MLD, which ranges in depth from 75 km to 130 km (MLD1) and is present mostly in regions P2 and P3. The deeper negative drop is interpreted as the LAB, which is found at depths of 200–259 km beneath the craton, and 60–150 km in the western region. Velocity profiles for stations located in the stable craton (SPMN, VIMO and FRB) have a sharp HVD at ∼150–170 km depth (MLD2), indicating the presence of an intra-lithospheric low velocity zone of significant thickness. The depth and extent of this low velocity zone is in general agreement with that found in long-range seismic profiles (Thybo and Perchuc, 1997). These authors also identified this zone as a zone of intense scattering, the origin of which is not yet fully understood. These mid-lithospheric features (MLD1 and MLD2) do not extend to the border region P3 (e.g. Q30A).

Interestingly at station FRB, which is located near the core of the NA craton (i.e. the Canadian shield), two additional intra-lithospheric velocity jumps are detected, at 160 km (MLD3), and 200 km depth (MLD4), respectively. The last and stronger drop in velocity occurs at 240 km depth and is interpreted as the LAB, in agreement with other studies of this part of the craton (e.g. Bastow et al., 2013).

In the stable part of the continent (P2), the corresponding depth variations in ξ show a change from $\xi > 1$ to moderately $\xi < 1$ in the depth range 150–250 km.

In contrast, for stations in P1, there is no detected MLD, but lithospheric thickness increases slightly from 60 km at 214A to 130 km in X23A, continuing to 170 km at Q30A (P3), which is the first station on this profile exhibiting MLD's and an intra-lithospheric low velocity zone. As already described above, the seismic structure at stations close to the Pacific coast shows complexity at depths grater than 130 km, suggesting the presence of

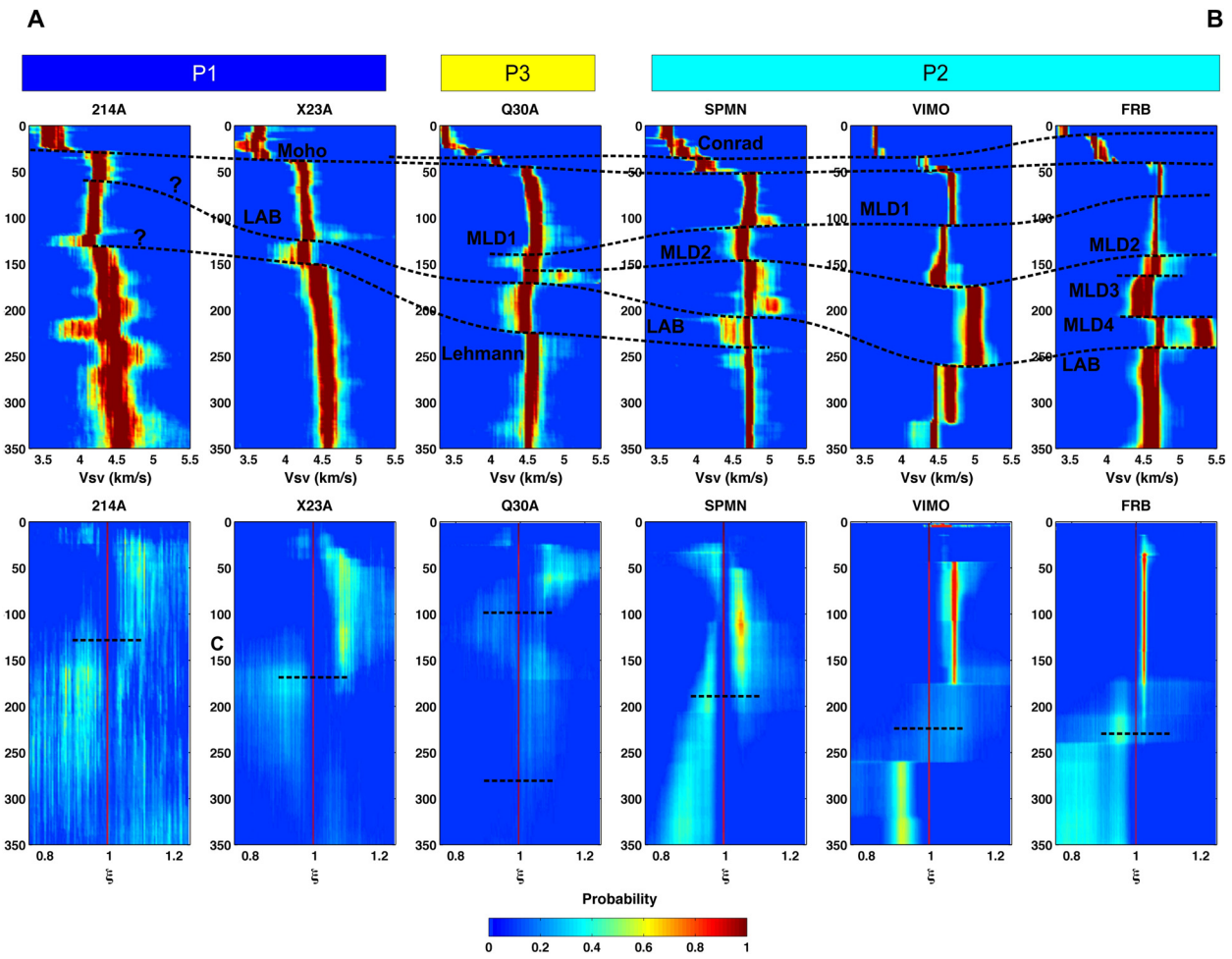

Fig. 7. 1D Posterior Density Distributions of V_{sv} (top) and ξ (bottom) at stations aligned along the profile A–B shown in Fig. 2. Dashed lines in V_{sv} connect the main variations in depth observed on the models and discussed in the text. Dashed lines in PPD of ξ roughly indicate the depth of change from $\xi > 1$ to $\xi < 1$.

strong heterogeneities in the region. The transition from $\xi > 1$ to $\xi < 1$ in P1 and P3 occurs at shallower depths (120–150 km) than in P2 as indicated by the dashed line in Fig. 7.

An increase in V_{sv} at depths of 150–230 km beneath P1 and P3 stations may represent the L discontinuity, which is not visible at stations within the northeast part of the craton (P2).

In Fig. 8, we present maps showing the topography of the clearest and well-documented discontinuities (Appendix 3). We also show the lateral variations in the depth of the transition from $\xi > 1$ to $\xi < 1$ (Fig. 8). The maps are built from the results obtained at each of the 30 stations, by interpolating the depth of each discontinuity on a 1×1 degree grid using a weighted-distance function. Fig. 8 shows that the trends discussed above can be generally extended to the whole NA continent and that the main features observed in the three provinces correspond well with the regionalization obtained from the tomographic model. The Moho is shallow in region P1 and reaches 50 km depth in P2. MLD's are mostly observed in P2 and P3 with the largest depths in the core of P2, for MLD1, and in northeastern part of the NA continent, for MLD2. These discontinuities are generally not observed in region P1, although they are observed at a pair of stations in the easternmost part of the RM front and in a portion of the northernmost Canada/Alaska.

The LAB deepens from 60–80 km near the west coast of NA, to 240–250 km beneath the Quebec and Hudson Bay region. Likewise, the positive discontinuity, which we associate with the L, starts at 120–150 km depth in P1, deepens to about 220 km in the central part of P2 and south P3, and reaches 250 km beneath the Quebec region. In contrast, it is not observed at stations located near Hudson Bay and in the northernmost Canadian Shield. Finally, the depth of the transition from $\xi > 1$ to $\xi < 1$ shows a pattern that does not follow the regionalization of the V_{sv}. Excluding the northernmost stations, stations falling in region P2 show a similar trend for this transition, with a relatively constant depth at about 190–210 km. The largest variations are observed in region P1. Stations located inland in the region of the Juan de Fuca subduction zone show that this change occurs at depths of at least 350 km, whereas it is between 100–150 km at the northernmost and southernmost limit of the subduction zone.

6. Discussion

The probabilistic profiles obtained with our technique show several interesting features in the NA upper mantle. In province P1, the Moho is relatively shallow (28–35 km) and the LAB is identified at depths of 60–130 km (Fig. 5 and Appendix 2). Interestingly, in Fig. 7, the 2D profile shows that the depth of the LAB increases eastward, from the coast toward the RMF. Stations near the west coast of NA show a complex pattern of the velocity profile with depth below the LAB (e.g. 214A), probably due to strong lateral variations in the deep structure. In contrast, stations located inland in P1 (X23A) present a relatively simple pattern at depths greater than 150 km exhibiting both a clear LAB and a deeper positive velocity jump at depths ranging from 150 to 250 km that we interpret as the L discontinuity. In contrast, when moving eastward on profile AB (or northward along the profile CD, Appendix 2) to-

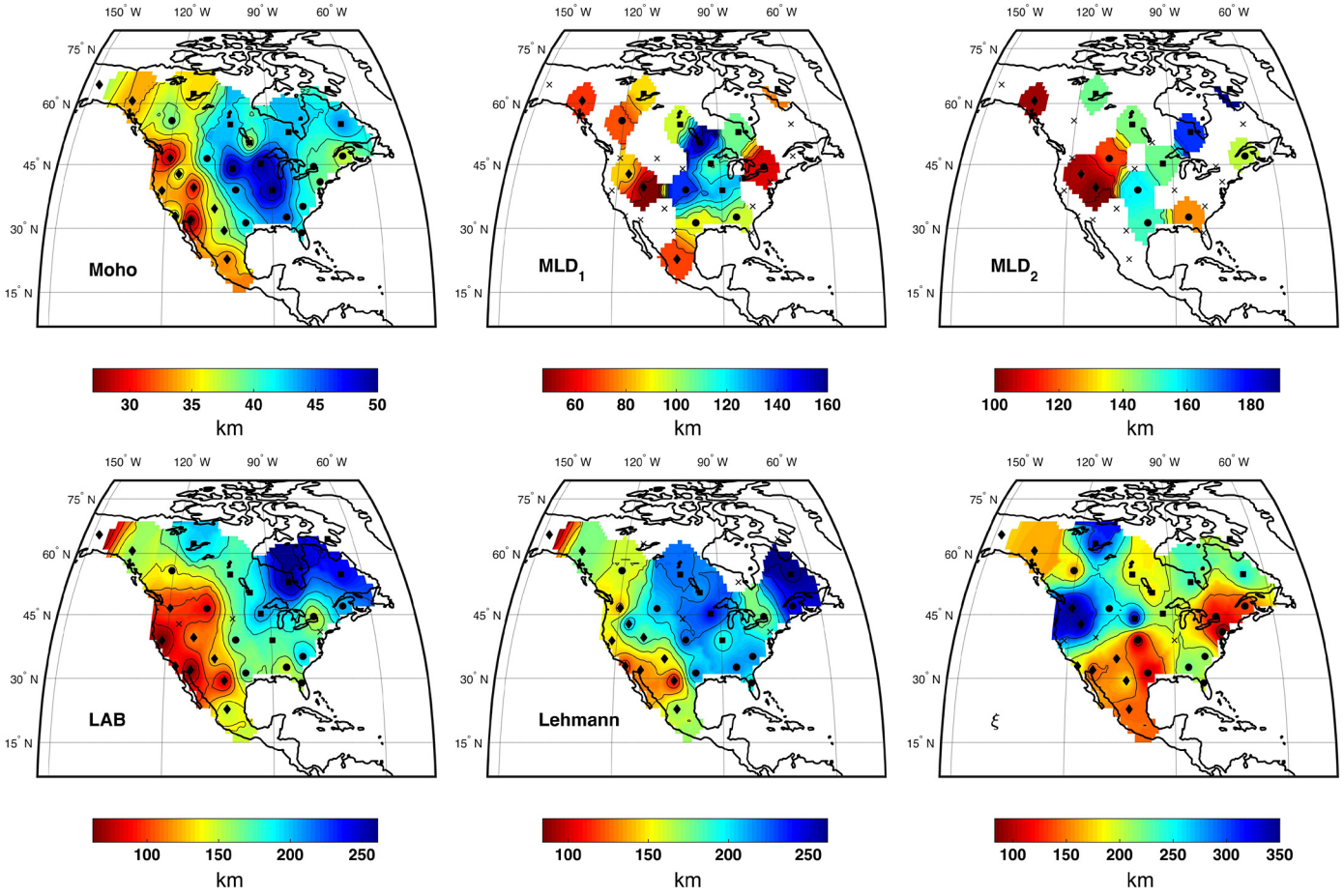

Fig. 8. Maps showing the depth distribution of the major discontinuities detected on the PPD. Stations located in P1, P2, P3, are indicated by diamonds, dots and squares, respectively. Crosses are the stations where no discontinuity is detected.

wards the craton through region P3, the L becomes deeper, and is generally no longer detected in the northernmost and easternmost regions. The lithosphere progressively thickens towards the craton interior (in profile AB, from 160 km at Q30A, and in profile CD from 170 km at Q43A, to 200–250 km further south), and one or more MLD's are present within it. Other studies based on the analysis of P-s and S-p receiver functions (Abt et al., 2010; Wirth and Long, 2014; Hansen et al., 2015) show strong layering in the first 200 km for longitudes east of 98°–95° W. Our profiles display similar features extending this pattern down to 300–350 km depth and clarifying the presence of alternating layers of faster and slower velocity within the mantle.

Some of the mechanisms proposed to explain the origin of MLDs involve the presence of fluids and carbon dioxide, allowing the presence of partial melt (e.g., Thybo and Perchuc, 1997). Others suggest changes in chemical composition (e.g., Abt et al., 2010; Yuan and Romanowicz, 2010; Foster et al., 2014), or sharp variations in the orientation of anisotropy (e.g., Rychert et al., 2010; Yuan and Romanowicz, 2010) or a peak in attenuation due to deformation accommodated by grain boundary sliding (Karato, 2012), or yet a remnant signature of old LAB formed when the lithosphere was young and active (Rader et al., 2015). However all these models focus on the sharp decrease in seismic velocity at depths of 100–130 km, and do not discuss the possible existence of a positive velocity jump in the depth range 150–250 km.

The alternation of negative and positive discontinuities observed in our models does not necessarily imply the presence of melt at these depths in this cold and stable province (Hansen et al., 2015). The increase in the number of layers in the north-central and eastern parts of NA, where the lithosphere reaches the largest thickness, suggests that the older the craton, the more layers there are, implying that thickening of the continental lithosphere with time occurred through some form of successive underplating, possibly via stacked slabs and/or arc accretion and underthrusting (e.g. Wirth and Long, 2014).

On the other hand, the presence of a clear L only under the western US is in contrast to the results of Gu et al. (2001), who, using SS precursors, reported the detection of the L in central and eastern north America, but not in the western tectonically active provinces. This could be due to the unexpected shallow depth of the L in the western region, or to the relatively small jump in velocity associated with the L in the central craton, as shown in our results.

Depth profiles of ξ show a transition from $\xi > 1$ to $\xi < 1$ at somewhat shallower depths in P1 (∼120–180 km), compared to P2 (∼200–300 km). In both provinces, $\xi > 1$ is generally found across the whole lithosphere and the asthenosphere or at least the upper part of the latter. The pattern observed for radial anisotropy beneath the craton is in agreement with previous studies of the region, with large variations in the depth extent where $\xi > 1$ (Yuan et al., 2014). In some cases, there are two maxima in radial anisotropy, a first one at crustal/Moho depths and a second one much deeper (e.g. P04C, P15A, E07A, K10A, for P1, FFC, I28A, VIMO, for P2, 150A, Q30A, E19A, NBC4 for P3). However, we note that the depth resolution in ξ is poorer than for V_{sv}, since it is only constrained by SWD data. Worth noting is the pattern observed for ξ inland of the Juan de Fuca subduction zone. In this region, we observe the largest depths of the ξ transition suggest-

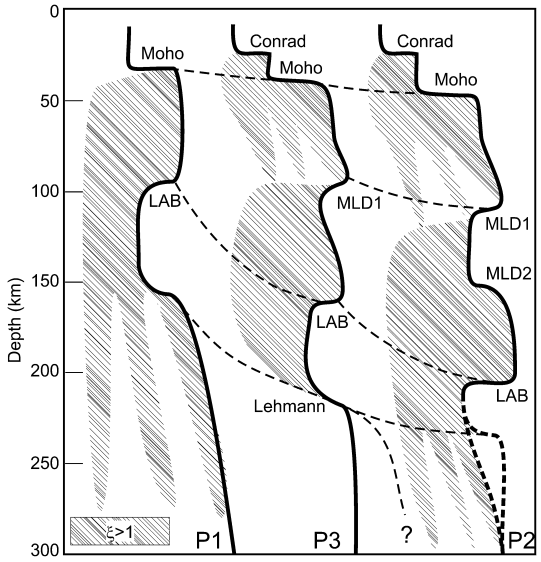

Fig. 9. Sketch showing the main contrasted features of regions P1, P2, and P3. 1) The crust thickens from P1 to P2, and a mid-lithospheric discontinuity appears in P3; 2) The LAB deepens from P1 to P2, with MLD's present in P3 but not in P1, and a positive discontinuity (Lehmann?) is present below the LAB. Radial anisotropy is characterized by $\xi > 1$ within the lithosphere and extending into the asthenosphere, with a change to $\xi < 1$ at depths ranging from 150–200 km in P1 to 200–300 km in P2 and P3. Forked parts indicate regions where, within the same province, differences of ξ are observed.

ing that ξ reflects processes within or around the subducted plate down to at least 350 km.

The main features that emerge from the analysis of the 30 1D profiles across NA are summarized in the form of a sketch in Fig. 9, where the main discontinuities observed in each of the 3 provinces are compared, together with the depth distribution of radial anisotropy.

7. Conclusions

We combined long and short period seismic observations in a Bayesian inversion scheme, and constrained upper-mantle layering beneath 30 stations distributed across the north American continent. Cluster analysis of a recent global velocity model provided an objective way to group stations into three provinces, according to similar tectonic features. In the western province (P1), the Moho is relatively shallow (25–35 km depth), as is the LAB (60–130 km depth) and there is a marked Lehmann discontinuity. In contrast, within the craton (P2), the crust is thick (up to 50 km) and a positive mid-crustal discontinuity (Conrad) exists. The LAB always occurs at depths greater than 170 km, in the craton, and at least two MLD's are found, at depths of about 100–130 and 150–170 km, marking the top and bottom of an intra-lithospheric low shear velocity zone, respectively. We note the strong layering in the lithosphere of the oldest part of the craton, suggesting thickening of the craton through successive underplating.

The L discontinuity is generally found at depths greater than 200 km, except in the central core of the craton where it is no longer observed. The RMF and southeastern US province (P3) show intermediate features with the presence of MLD, LAB, and L discontinuities. Many of these features have been previously observed in different RF studies, but the addition of surface wave constraints in a consistent Bayesian framework allows the construction of absolute velocity (and radial anisotropy) depth profiles, and brings out first order features with improved clarity, providing a proof-of-concept for this approach, which we plan to extend to a larger number of stations in the near future.

Acknowledgements

Computations were performed at the Los Alamos National Laboratory computational facility. We acknowledge support from the "UC Lab-fee" research collaboration program (UCOP grant 12-LR-236345) conducted in collaboration with M. Maceira and C. Larmat at Los Alamos National Laboratory, and NSF Earthscope grant EAR-1460205. T. Bodin wishes to acknowledge support from the Miller Institute for Basic Research at the University of California, Berkeley.

Appendix A. Supplementary material

Supplementary material related to this article can be found online at http://dx.doi.org/10.1016/j.epsl.2016.05.054.

References

Abt, D.L., Fischer, K.M., French, S.W., Ford, H.A., Yuan, H., Romanowicz, B., 2010. North American lithospheric discontinuity structure imaged by Ps and Sp receiver functions. J. Geophys. Res. 115, B09301. http://dx.doi.org/10.1029/2009JB006914.

Agrawal, M., Pulliam, J., Sen, M.K., Dutta, U., Pasyanos, M.E., Mellors, R., 2015. Crustal and uppermost mantle structure in the Middle East: assessing constraints provided by jointly modelling Ps and Sp receiver functions and Rayleigh wave group velocity dispersion curves. Geophys. J. Int. 201 (2), 783–810. http://dx.doi.org/10.1093/gji/ggv050.

Ammon, C.J., Randall, G.E., Zandt, G., 1990. On the nonuniqueness of receiver function inversions. J. Geophys. Res. 95, 15 303 ± 15 318.

Bastow, I.D., Eaton, D.W., Kendall, J.-M., Helffrich, G., Snyder, D.B., Thompson, D.A., Wookey, J., Darbyshire, F.A., Pawlak, A.E., 2013. The Hudson Bay Lithospheric Experiment (HuBLE): insights into Precambrian plate tectonics and the development of mantle keels. Geol. Soc. (Lond.) Spec. Publ. 389, 41–67. http://dx.doi.org/10.1144/SP389.7.

Bianchi, I., Park, J., Piana Agostinetti, N., Levin, V., 2010. Mapping seismic anisotropy using harmonic decomposition of receiver functions: an application to Northern Apennines, Italy. J. Geophys. Res. 115, B12317. http://dx.doi.org/10.1029/2009JB007061.

Bodin, T., Sambridge, M., Tkalčíc, H., Arroucau, P., Gallagher, K., Rawlinson, N., 2012. Transdimensional inversion of receiver functions and surface wave dispersion. J. Geophys. Res. 117 (B02), 301. http://dx.doi.org/10.1029/2011JB008560.

Bodin, T., Yuan, H., Romanowicz, B., 2014. Inversion of receiver functions without deconvolution. Geophys. J. Int. 196 (2), 1025–1033.

Bodin, T., Capdeville, Y., Romanowicz, B., Montagner, J.P., 2015. Interpreting radial anisotropy in global and regional tomographic models. Book chapter. In: Khan, A., Deschamps, F., Kawai, K. (Eds.), The Earth's Heterogeneous Mantle. Springer International Publishing.

Bodin, T., Leiva, J., Romanowicz, B., Maupin, V., Yuan, H., 2016. Imaging anisotropic layering with Bayesian inversion of multiple data types. Geophys. J. Int. http://dx.doi.org/10.1093/gji/ggw124.

Bostock, M.G., 1998. Mantle stratigraphy and evolution of the Slave province. J. Geophys. Res. 103, 21,183–21,200. http://dx.doi.org/10.1029/98JB01069.

Dettmer, J., Dosso, S., Bodin, T., Stipcevic, J., Cummins, P., 2015. Direct seismogram inversion for receiver-side structure with uncertain source-time functions. Geophys. J. Int. 203 (2), 1373–1387. http://dx.doi.org/10.1093/gji/ggv375.

Ekström, G., 2011. A global model of Love and Rayleigh surface wave dispersion and anisotropy, 25–250 s. Geophys. J. Int. 187, 1668–1686. http://dx.doi.org/10.1111/j.1365-246X.2011.05225.x.

Foster, K., Dueker, K., Schmandt, B., Yuan, H., 2014. A sharp cratonic lithosphere–asthenosphere boundary beneath the American Midwest and its relation to mantle flow. Earth Planet. Sci. Lett. 402, 82–89.

French, S., Romanowicz, B., 2014. Whole mantle radially anisotropic shear–velocity structure from spectral-element waveform tomography. Geophys. J. Int. 199, 1303–1327.

Girardin, N., Farra, V., 1998. Azimuthal anisotropy in the upper mantle from observation of P-to-S converted phases: application to southeast Australia. Geophys. J. Int. 133, 615–629.

Green, P., 1995. Reversible jump MCMC computation and Bayesian model selection. Biometrika 82, 711–732.

Gu, Y.J., Dziewonski, A.M., Ekström, G., 2001. Preferential detection of the Lehmann discontinuity beneath continents. Geophys. Res. Lett. 28, 4655–4658.

Hales, A.L., 1969. A seismic discontinuity in the lithosphere. Earth Planet. Sci. Lett. 7, 44–46. http://dx.doi.org/10.1016/0012-821X(69)90009-0.

Hansen, S.M., Dueker, K., Schmandt, B., 2015. Thermal classification of lithospheric discontinuities beneath USArray. Earth Planet. Sci. Lett. 431 (1), 36–47. http://dx.doi.org/10.1016/j.epsl.2015.09.009.

Julià, J., Ammon, C.J., Herrmann, R.B., Correig, A.M., 2000. Joint inversion of receiver function and surface wave dispersion observations. Geophys. J. Int. 143, 99–112. http://dx.doi.org/10.1046/j.1365-246x.2000.00217.x.

Karato, S.I., 2012. On the origin of the asthenosphere. Earth Planet. Sci. Lett. 321, 95–103.

Kumar, P., Kind, R., Yuan, X., Mechie, J., 2012. USArray receiver function images of the lithosphere–asthenosphere boundary. Seismol. Res. Lett. 83, 486–491.

Kustowski, B., Ekström, G., Dziewoński, A.M., 2008. STW105 and S362ANI: anisotropic shear-wave velocity structure of the Earth's mantle: a global model. J. Geophys. Res. 113, B06306. http://dx.doi.org/10.1029/2007JB005169.

Lehmann, I., 1961. S and the structure of the upper mantle. Geophys. J. R. Astron. Soc. 4, 124–138.

Lekic, V., Romanowicz, B., 2011. Tectonic regionalization without a priori information: a cluster analysis of upper mantle tomography. Earth Planet. Sci. Lett. 308, 1–2, 1, 151–160.

Leven, J.H., Jackson, I., Ringwood, A.E., 1981. Upper mantle seismic anisotropy and lithospheric decoupling. Nature 289, 234–239.

Levin, V., Park, J., 1998. P-SH conversions in layered media with hexagonally symmetric anisotropy: a cookbook. Pure Appl. Geophys. 151 (2–4), 669–697.

Malinverno, A., Briggs, V., 2004. Expanded uncertainty quantification in inverse problems: hierarchical Bayes and empirical Bayes. Geophysics 69, 1005.

Marone, F., Romanowicz, B., 2007. The depth distribution of azimuthal anisotropy in the continental upper mantle. Nature 447 (7141), 198–201.

Menke, W., Levin, V., 2003. The cross-convolution method for interpreting sks splitting observations, with application to one and two-layer anisotropic earth models. Geophys. J. Int. 154 (2), 379–392.

Mueller, S., Landisman, M., 1966. Seismic studies of the Earth's crust in continents I: evidence for a low-velocity zone in the upper part of the lithosphere. Geophys. J. R. Astron. Soc. 10, 525–538.

Nettles, M., Dziewoński, A.M., 2008. Radially anisotropic shear velocity structure of the upper mantle globally and beneath North America. J. Geophys. Res. 113, B02303. http://dx.doi.org/10.1029/2006JB004819.

Panning, M.P., Romanowicz, B., 2006. A three dimensional radially anisotropic model of shear velocity in the whole mantle. Geophys. J. Int. 167, 361–379.

Rader, E., Emry, E., Schmerr, N., Frost, D., Cheng, C., Menard, J., Yu, C.Q., Geist, D., 2015. Characterization and petrological constraints of the midlithospheric discontinuity. Geochem. Geophys. Geosyst. 16, 3484–3504. http://dx.doi.org/10.1002/2015GC005943.

Ritsema, J., van Heijst, H.J., Deuss, A., Woodhouse, J.H., 2011. S40RTS: a degree-40 shear velocity model for the mantle from new Rayleigh wave dispersion, teleseismic traveltimes, and normal-mode splitting function measurements. Geophys. J. Int. 184. http://dx.doi.org/10.1111/j.1365-246X.2010.04884.x.

Rychert, C.A., Shearer, P.M., Fischer, K.M., 2010. Scattered wave imaging of the lithosphere–asthenosphere boundary. Lithos 120, 173–185.

Sambridge, M., Mosegaard, K., 2002. Monte Carlo methods in geophysical inverse problems. Rev. Geophys. 40 (3), 3-1–3-29.

Schaeffer, A.J., Lebedev, S., 2014. Imaging the North American continent using waveform inversion of global and USArray data. Earth Planet. Sci. Lett. 402, 26–41.

Shapiro, N.M., Ritzwoller, M.H., 2002. Monte-Carlo inversion for a global shear velocity model of the crust and upper mantle. Geophys. J. Int. 151, 88–105.

Shearer, P.M., 1991. Constraints on upper mantle discontinuities from observations of long-period reflected and converted phases. J. Geophys. Res. 96 (B11), 18147–18182. http://dx.doi.org/10.1029/91JB01592.

Shen, W., Ritzwoller, M.H., Schulte-Pelkum, V., 2013. A 3-D model of the crust and uppermost mantle beneath the central and western US by joint inversion of receiver functions and surface wave dispersion. J. Geophys. Res. 118 (1), 262–272. http://dx.doi.org/10.1029/2012JB009602.

Takeuchi, H., Saito, M., 1972. Seismic surface waves. Methods Comput. Phys. 11, 217–295.

Thybo, H., Perchuc, E., 1997. The seismic 8° discontinuity and partial melt in the continental mantle. Science 275, 1626–1629. http://dx.doi.org/10.1126/science.275.5306.1626.

van der Lee, S., Frederiksen, A., 2005. Surface wave tomography applied to the North American upper mantle. In: Levander, A., Nolet, G. (Eds.), AGU Monograph "Seismic Earth: Array Analysis of Broadband Seismograms", pp. 67–80.

Vinnik, L.P., 1977. Detection of waves converted from P to SV in the mantle. Phys. Earth Planet. Inter. 15, 39–45.

Vinnik, L., Kurnik, E., Farra, V., 2005. Lehmann discontinuity beneath North America: no role for seismic anisotropy. Geophys. Res. Lett. 32, L09306. http://dx.doi.org/10.1029/2004GL022333.

Yuan, H., Romanowicz, B., 2010. Lithospheric layering in the North American Craton. Nature 466, 1063–1069.

Yuan, H., French, S., Cupillard, P., Romanowicz, B., 2014. Lithospheric expression of geological units in central and eastern North America from full waveform tomography. Earth Planet. Sci. Lett. 402, 176–186. http://dx.doi.org/10.1016/j.epsl.2013.11.057.

Whitmeyer, S.J., Karlstrom, K.E., 2007. Tectonic model for the Proterozoic growth of North America. Geosphere 3, 220–259.

Wirth, E.A., Long, M.D., 2014. A contrast in anisotropy across mid-lithospheric discontinuities beneath the central United States—a relic of craton formation. Geology 42, 851–854. http://dx.doi.org/10.1130/G35804.1.